Journal of Sound and Vibration 494 (2021) 115896

Contents lists available at ScienceDirect

Journal of Sound and Vibration

journal homepage: www.elsevier.com/locate/jsv

Three dimensional aeroelastic analyses considering free-play nonlinearity using computational fluid dynamics/computational structural dynamics coupling

Chengde Huang[a], Jie Huang[a,b], Xin Song[a,b], Guannan Zheng[a,b], Guowei Yang[a,b,*]

[a] LMFS of Institute of Mechanics, Chinese Academy of Sciences, Beijing 100190, China
[b] School of Engineering Science, University of Chinese Academy of Sciences, Beijing 100049, China

ARTICLE INFO

Article history:
Received 15 May 2020
Revised 2 December 2020
Accepted 2 December 2020
Available online 3 December 2020

Key words:
Free-play
Transonic dip
Flutter
Limit cycle oscillation
Aeroelastic

ABSTRACT

Most of the previous studies on free-play aeroelasticity were based on the linear aerodynamic theory, which cannot consider the aerodynamic nonlinear effects. This paper proposes a framework of computational fluid dynamics/computational structural dynamics (CFD/CSD) coupling approach that can deal with the three dimensional aeroelastic problems with both the free-play nonlinearity and the aerodynamic nonlinearity. The fictitious mass method is used to construct the reduced structural equations of motion and the switching point is detected using the bisection method. The adaptive time step obtained by the bisection method is returned to the CFD solver so that both the structural and the fluid equations are integrated using the same time step. An all-movable wing with free-play at the root is considered for numerical studies. Results demonstrate the CFD/CSD coupling method can predict the stable limit cycle oscillation (LCO) effectively. The initial condition study shows that the LCO behavior is subcritical and the hysteresis response can be predicted in time domain effectively by the presented method. The viscous effect is shown to increase the LCO boundary and shift the LCO amplitude to a larger velocity in transonic regime. The LCO boundary is determined from subsonic to transonic Mach numbers. The transonic dip in LCO boundary is found by the CFD/CSD coupling method, but the equivalent linearization with doublet lattice method fails to predict this phenomenon. From the results of this study, the LCO boundary is shown to be 43.5% below the flutter boundary at most.

1. Introduction

The free-play nonlinearity is usually caused by wear and manufacturing tolerances in the linkage where relative motions exist [1]. This nonlinearity is piecewise linear and non-smooth as illustrated with Fig. 1. It can induce limit cycle oscillations (LCOs) even if the flow velocity is less than the linear flutter speed. LCOs have negative effects on pilot handling quality, human comfort, structural fatigue and so on [2].

The describing function method (DFM, also called the equivalent linearization method) has been extensively applied to the free-play aeroelastic analyses [3–10]. Once the static equilibrium position and the LCO amplitude are given, DFM can

* Corresponding author.
E-mail addresses: huangchengde@imech.ac.cn (C. Huang), zhengguannan@imech.ac.cn (G. Zheng), gwyang@imech.ac.cn (G. Yang).

https://doi.org/10.1016/j.jsv.2020.115896
0022-460X/

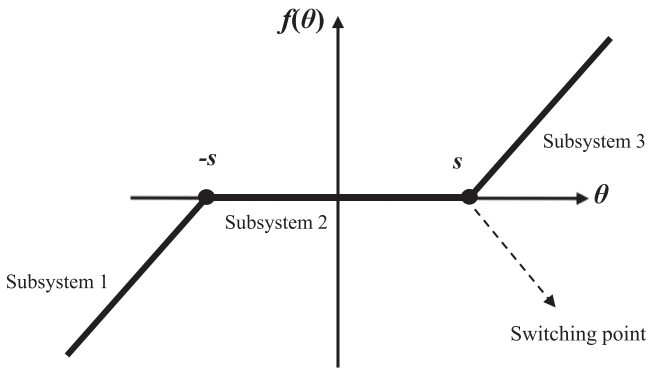

Fig. 1. Free-play nonlinearity.

obtain the equivalent linearized stiffness under the assumption of harmonic motion. Then, conventional flutter prediction methods such as the p-k method or V-g method can be used to calculate the flutter speed so that the relationship between the LCO amplitude and flow velocity can be obtained. Gordon et al. [7] used DFM and the Theodorsen aerodynamic theory to study the stable and unstable LCOs of a typical-section airfoil with free-play. Lee and Tron [8] used the doublet lattice method (DLM) and DFM to calculate the nonlinear flutter speed of the folding wing of CF-18 aircraft with free-play. Kholodar [9] studied the effect of preload using DFM. The results showed a certain amount of preload could cause the change in equivalent stiffness which might lead to high-frequency oscillations, but a sufficient amount of preload could suppress the oscillations. Yang et al. [10] generalized DFM to the aerodynamic force based on Euler equations. In their work, the aerodynamic and structural describing functions were calculated, and then the V-g method was used to analyze the LCO behaviors. DFM only considers the first-order harmonic, while the high order harmonic balance method (HOHBM) retains high order harmonics and can be applied to the general periodic responses [11,12]. Liu and Dowell [13], Fichera and Ricci [14] used HOHBM to study the LCOs induced by free-play nonlinearity. The results indicated HOHBM could improve the numerical accuracy compared with DFM.

Detailed information of the responses can only be obtained by time domain methods, which are suitable for the analyses of complex aeroelastic phenomena such as chaotic motions. For a two-dimensional (2-D) aeroelastic system that only has several degrees-of-freedom (DOFs), it is convenient to construct the free-play aeroelastic system in terms of physical coordinates. For example, Dai et al. [15] studied the aeroelastic behaviors of an airfoil with free-play in pitch using a two-DOF structural equations of motion. The Theodorsen aerodynamic theory was utilized along with the Wagner function to calculate the unsteady aerodynamic forces. Both LCOs and chaotic motions were observed in their work. The 2-D problems were also studied by many other researchers [16–19] and the analysis method could be generalized to three-dimensional (3-D) rigid wings. Firouz-Abadi et al. [20] considered a 3-D rigid fin that could plunge, pitch and flap. Each of the DOFs was constrained by a free-play spring and the aeroelastic responses were simulated in supersonic flows based on the shock-expansion theory and the local piston theory.

However, if the 3-D wing is elastic, both the stiffness of the wing and the connection stiffness at the free-play hinge should be considered. Using the original physical coordinates to construct the aeroelastic system will result in a large amount of computational cost, to reduce which modal approaches are preferred [21–27]. For example, Kim et al. [22] employed the component mode synthesis method to analyze the nonlinear dynamic behaviors of a deployable missile control fin with nonlinear hinge. In their work, the fin was divided into two substructures that were connected at the hinge. The displacements were represented by a linear combination of the modes for each substructure, while the compatibility condition along the substructure boundaries took the nonlinear hinge into account. Yang et al. [23] coupled the component mode synthesis method and the aerodynamic potential theory to perform nonlinear flutter analyses of a folding fin with free-play in subsonic flows. Wind tunnel tests were also carried out and the trend of divergent speed was the same between the calculated and measured results.

It is another choice to use a constant modal space. As shown in Fig. 1, the free-play nonlinear system consists of three linear subsystems. Once the subsystem is changed, the natural modes that span the modal space are also changed. Changing the modes repeatedly will produce the errors coming from the coordinate transformation between different modal spaces. To avoid this problem, a constant modal basis can be used such as the residual modes [24,25] and the fictitious mass (FM) modes [26,27].

In this work, the FM method is discussed which was proposed by Karpel and Wiesemanm [26,27]. The idea is that the local stiffness variations can be properly considered by the modes containing local significant deformations. This kind of modes can be obtained by adding a large mass to the local DOF. The FM method has proved to be effective for the dimensionality reduction of the free-play nonlinear system and has been adopted by previous researchers [28–35]. For example, Huang et al. [28] used the FM method and the aerodynamic potential theory to analyze the aeroservoelastic behaviors of a 3-D wing with two free-play control surfaces. Bae et al. [29] studied the free-play aeroelastic responses based on the FM

method and pointed out that the time domain method could predict chaotic motions that could not be analyzed by the frequency domain method.

Most of the previous 3-D cases were analyzed using the linear aerodynamic theory, which cannot consider aerodynamic nonlinearities such as the transonic flows. On the other hand, the application of computational fluid dynamics was mainly restricted to 2-D cases [10,36–39]. Since the free-play nonlinearity can cause LCOs below the flutter boundary, its effect on transonic dip phenomenon needs to be evaluated. What's more, it remains a challenge to detect the switching points for a 3-D structure with free-play. Now that the 3-D problems considering both the free-play and aerodynamic nonlinearities were seldom discussed, it is necessary to develop a 3-D computational fluid dynamics/computational structural dynamics (CFD/CSD) coupling method to analyze the aeroelastic behaviors and predict the stability boundary of free-play aeroelastic systems.

This paper is organized as follows. Section 2 constructs the numerical framework. In Section 3, an all-movable wing is considered for numerical studies. The LCO prediction, LCO boundary, viscous effect, hysteresis phenomenon and transonic dip phenomenon are discussed. Finally, Section 4 describes the conclusions.

2. Numerical approach

2.1. Fictitious mass method

For a nonlinear aeroelastic problem, the structural equations of motion without damping are expressed as:

$$\mathbf{M}\ddot{\mathbf{u}} + \mathbf{R}(\mathbf{u}) = \mathbf{F} \tag{1}$$

where $\boldsymbol{M}$, $\boldsymbol{F}$, $\boldsymbol{u}$, $\boldsymbol{R}(\boldsymbol{u})$ denote the mass matrix, aerodynamic force vector, displacement vector and nonlinear restoring force vector, respectively. For a concentrated nonlinearity, the nonlinear restoring force vector is as follows:

$$\mathbf{R}(\mathbf{u}) = \mathbf{K}\mathbf{u} + \mathbf{P}f(\theta) \tag{2}$$

where $\boldsymbol{K}$ is the linear stiffness matrix, $f(\theta)$ denotes the restoring force of a nonlinear spring at the hinge, $\boldsymbol{P}$ stands for the chosen matrix which is a sparse matrix and the nonzero element only exists at the connection DOF of the hinge. The free-play nonlinear system is piecewise linear and can be divided into three linear subsystems (Fig. 1), so the restoring force is expressed as:

$$f(\theta) = \begin{cases} k(\theta + s), & \theta < -s \\ 0, & -s < \theta < s \\ k(\theta - s), & \theta > s \end{cases} \tag{3}$$

In the FM method, the nonlinear spring is replaced by a large mass (also called the fictitious mass) at the connection DOF to calculate the FM modes. Then the FM modes can be obtained by the following eigenvalue problem:

$$\left[\mathbf{K} - \omega_{\mathrm{f}}^2(\mathbf{M} + \mathbf{M}_{\mathrm{f}})\right]\boldsymbol{\varphi}_{\mathrm{f}} = \mathbf{0} \tag{4}$$

where $\boldsymbol{M}_{\mathrm{f}}$ denotes the FM matrix and is also sparse, $\boldsymbol{\varphi}_{\mathrm{f}}$ and ω_{f} denote the FM mode shape and frequency, respectively. The FM modes are normalized so that

$$\boldsymbol{\Phi}_{\mathrm{f}}^{\mathrm{T}}(\mathbf{M} + \mathbf{M}_{\mathrm{f}})\boldsymbol{\Phi}_{\mathrm{f}} = \mathbf{I}, \quad \boldsymbol{\Phi}_{\mathrm{f}}^{\mathrm{T}}\mathbf{K}\boldsymbol{\Phi}_{\mathrm{f}} = \boldsymbol{\Lambda}_{\mathrm{f}} \tag{5}$$

where $\boldsymbol{\Phi}_{\mathrm{f}}$, $\boldsymbol{\Lambda}_{\mathrm{f}}$, $\boldsymbol{I}$ denote the FM modal matrix, spectral matrix and identify matrix, respectively. The FM modes contain local deformations near the free-play hinge so that the modes can serve as a constant set of basis vectors for the piecewise linear system [27]. The displacements of the free-play nonlinear system can be expressed as a linear combination of the FM modes:

$$\mathbf{u} = \boldsymbol{\Phi}_{\mathrm{f}}\boldsymbol{\eta} \tag{6}$$

where $\boldsymbol{\eta}$ denotes the generalized displacements. Because the rotational angle θ needs to be calculated, the modal matrix should contain rotational components.

Substituting Eq. (6) into Eq. (1) with the aid of Eqs. (2) and (5) yields the reduced structural equations of motion:

$$\mathbf{M}_{\mathrm{g}}\ddot{\boldsymbol{\eta}} + \boldsymbol{\Lambda}_{\mathrm{f}}\boldsymbol{\eta} + \boldsymbol{\Phi}_{\mathrm{f}}^{\mathrm{T}}\mathbf{P}f(\theta) = \mathbf{F}_{\mathrm{g}} \tag{7}$$

where,

$$\begin{aligned} \mathbf{M}_{\mathrm{g}} &= \mathbf{I} - \boldsymbol{\Phi}_{\mathrm{f}}^{\mathrm{T}}\mathbf{M}_{\mathrm{f}}\boldsymbol{\Phi}_{\mathrm{f}} \\ \mathbf{F}_{\mathrm{g}} &= \boldsymbol{\Phi}_{\mathrm{f}}^{\mathrm{T}}\mathbf{F} \end{aligned} \tag{8}$$

in which subscript "g" denotes the generalized matrixes. Note that the generalized aerodynamic force $\boldsymbol{F}_{\mathrm{g}}$ and the rotational angle θ are functions of $\boldsymbol{\eta}$. Eq. (7) is marched in time using the fourth-order Runge-Kutta (RK4) method based on adaptive time step. The adaptive approach is discussed in Section 2.2.

2.2. Catching the switching point

As shown in Fig. 1, there are two switching points resulting in the non-smoothness of the free-play system. Integrating the structural equations using a fixed time step is incapable of catching the switching points accurately. The round-off error will grow with time marching and finally may lead to numerical instability [40]. To overcome this difficulty, the time step should be adapted elaborately to locate the switching points.

There are some time marching methods that can integrate to the switching points accurately, such as the predictor-corrector algorithm [41,42], the Henon's method [15,40] and the point transformation method [13,43]. However, all these methods are only suitable for the systems having several DOFs in which the rotational angle explicitly exists, and require that the aerodynamic model has analytic expressions. So far, these methods are only applied to 2-D aeroelastic systems in incompressible flow and it is difficult to generalize them to 3-D aeroelastic systems in general flow conditions.

In the present work, the bisection method is developed to deal with this problem. This method is suitable for 3-D problems and it ensures high accuracy for catching the switching points. The procedure is as follows.

(1) First of all, define a normal time step Δt_{n}.
(2) Integrate the structural equations from t to $t + \Delta t_{\mathrm{n}}$ and calculate the rotational angle θ at the hinge. The computation of θ is based on the linear combination of FM modes. If the subsystem does not change, then continue the time marching using the step of Δt_{n}. Otherwise, the step should be adjusted and go to (3).
(3) Define the function $f(t) = \theta(t) - s$, where s denotes the switching point crossed, and define a tolerance $\varepsilon = 10^{-10}$.
(4) Let $a = 0$, $b = \Delta t_{\mathrm{n}}$. If $|f(t+b)| < \varepsilon$, then return b as the adaptive time step and go to (7). Otherwise, go to (5).
(5) Let $c = (a+b)/2$. Integrate the structural equations from t to $t + c$ and recalculate the rotational angle θ. If $|f(t+c)| < \varepsilon$, then return c as the adaptive time step and go to (7). Otherwise, go to (6).
(6) If $f(c) \cdot f(b) < 0$, let $a = c$, otherwise let $b = c$. Go to (5).
(7) Go to (2) for the next time step.

2.3. Aerodynamic solver

ANSYS FLUENT is used for the unsteady aerodynamic simulations. The governing equations are three-dimensional compressible Navier–Stokes (N-S) equations. The gradients are evaluated by the Green-Gauss scheme and the vector of convective fluxes is evaluated by the Roe-FDS scheme. The Sutherland formula is used to calculate the molecular viscosity coefficient, and the turbulence is simulated using the shear-stress transport (SST) k-ω model. The second-order upwind scheme is used for the spatial discretizations of the flow and the turbulent variables. The implicit dual-time formulation is employed to integrate the equations in time.

2.4. Fluid-structure interpolation

In order to calculate the generalized aerodynamic forces $\boldsymbol{F}_{\mathrm{g}}$, the FM modes on the structural nodes should be first interpolated onto the aerodynamics nodes on the surface. In this paper, the radial basis function (RBF) method [44] is used for the interpolations. This method is based on the spatial positions of nodes only and can be performed on arbitrary point clouds with no connectivity information required. Moreover, only simple matrix operations are required. The general form of RBF interpolation is [45]:

$$s(\mathbf{x}) = \gamma_0 + \gamma_1 x + \gamma_2 y + \gamma_3 z + \sum_{i=1}^{N} \alpha_i \phi(\|\mathbf{x} - \mathbf{x}_i\|) \tag{9}$$

where $\boldsymbol{x} = (x, y, z)$, $\|\boldsymbol{x} - \boldsymbol{x}_i\|^2 = (x - x_i)^2 + (y - y_i)^2 + (z - z_i)^2$, and N is the number of control points. After the coefficients in Eq. (9) are calculated based on the known values at the control points, the substitution of a new point $\boldsymbol{x}$ into Eq. (9) yields the interpolated value. The Wendland's C2 function [44,46], which gives satisfactory interpolation accuracy, is chosen here:

$$\phi(\|\mathbf{x} - \mathbf{x}_i\|) = \begin{cases} (1 - \|\mathbf{x} - \mathbf{x}_i\|/d)^4 (4\|\mathbf{x} - \mathbf{x}_i\|/d + 1), & \|\mathbf{x} - \mathbf{x}_i\| \le d \\ 0\,, & \|\mathbf{x} - \mathbf{x}_i\| > d \end{cases} \tag{10}$$

where d represents the support radius and is chosen to be a suitable value to consider enough points near the interface and exclude the points far away [47].

The deflection of fluid-structure interface requires the update of the volume mesh according to the structural displacements evaluated by Eq. (6) using the generalized displacement vector $\boldsymbol{\eta}$. Mesh deformation is the preferred choice to update the CFD mesh automatically. The RBF method can also be used to deform the mesh. This method is mesh type independent and has proven to preserve the grid quality well [44]. However, selecting all the surface points as control points will make calculations expensive. To reduce the computational cost, Rendall and Allen [48] proposed the 'greedy' algorithm to reduce the number of the control points, which sacrifices the accuracy of the deformation on the surface with an acceptable error. In the present work, the RBF method is utilized along with the 'greedy' algorithm to deform the CFD volume mesh.

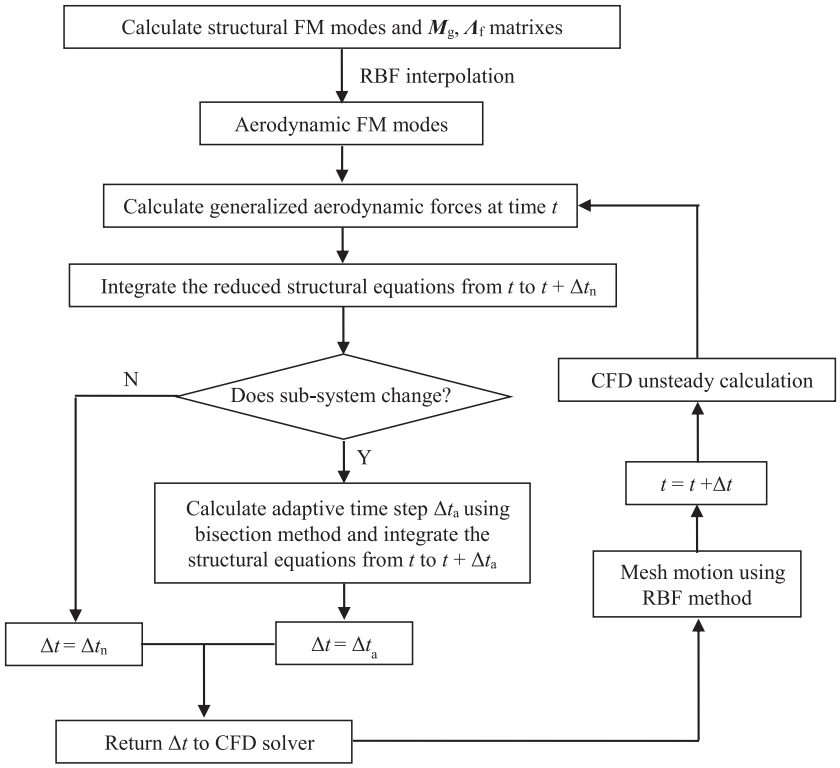

Fig. 2. Flowchart of CFD/CSD coupling for free-play aeroelastic simulations.

2.5. Implementation of CFD/CSD coupling

The flowchart of the proposed CFD/CSD coupling method is shown in Fig. 2. The three dimensional CFD mesh and the structural finite element model should be built and a normal time step Δt_n is defined in advance. In pre-processing, the structural FM modes are calculated which are then interpolated onto the aerodynamic nodes using RBF method. During the time simulation, the reduced structural equations and the CFD solver are coupled in a loosely coupling manner. After the calculation of unsteady aerodynamic force is converged at time t, the reduced structural equations are integrated in time. If the change in sub-system occurs, the bisection method is used to catch the switching point and determine the adaptive time step which is returned to the CFD solver so that both the structural and the fluid equations are integrated using the same time step. The volume mesh is deformed using the RBF method and then the unsteady aerodynamic force at next time step is calculated. This procedure is repeated so that the aeroelastic time response can be obtained.

In this paper, ANSYS FLUENT is chosen as the CFD solver. For free-play aeroelastic simulations, the FM method, the bisection method, the fluid-structure interpolation and mesh deformation schemes based on the RBF method are coded using the C programming language. Then, these codes are embedded into ANSYS FLUENT through user-defined functions to extend its range of application.

3. Results and discussions

3.1. Model descriptions

An all movable wing [34,35] is considered here as shown in Fig. 3. The structural thickness, the root chord length and the tip chord length are 0.002 m, 0.156 m and 0.078 m, respectively. The material is an Aluminum alloy. The Young's modulus, shear modulus and density are 72.4 GPa, 26.2 GPa and 2713 kg/m^3, respectively. The pitching axis is located in the mid-chord of the root. The free-play at the pitching axis is considered here. Within the free-play zone the hinge stiffness is zero, otherwise the hinge stiffness takes a normal value of 100 Nm/rad.

The airfoil section is NACA 0012. The viscous structured mesh is generated with clustered boundary layer cells. The number of volume cells is 0.82 million and the initial cell height near the wall is set to 1×10^{-6} m so that $y^+ < 1$. The CFD mesh distribution is shown in Fig. 4.

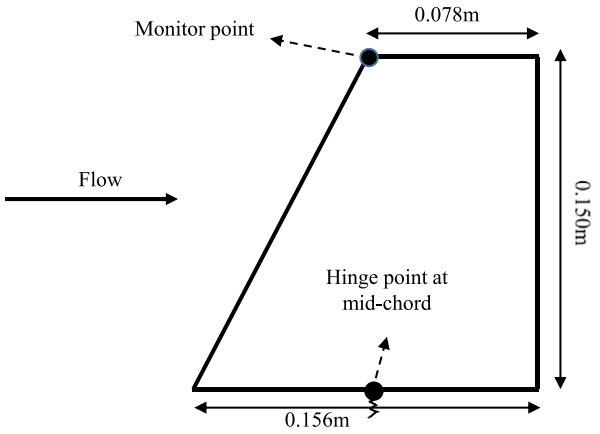

Fig. 3. The all-movable wing.

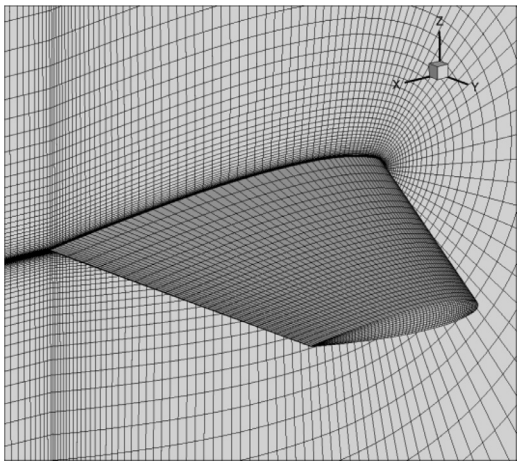

Fig. 4. CFD mesh on the surface and symmetry plane.

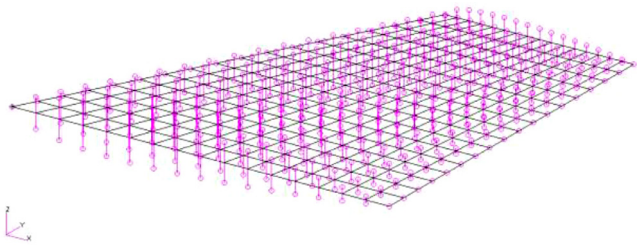

Fig. 5. Structural finite element model.

The structural finite element model is built using 16*17=272 quadrilateral shell elements as shown in Fig. 5. Note that the nodes of the shell elements are distributed on the mid-plane. To generate the wing section, the structural nodes on the wing surface are created and these nodes are connected to the mid-plane by the RBE2 elements in MSC.NASTRAN.

3.2. Linear structural and aeroelastic analyses

3.2.1. Natural modes

In this paper, the all movable wing is three-dimensional and elastic. Since the local stiffness at the hinge varies according to the structural responses, the conventional natural modes that consider a single fixed stiffness are not accurate enough for the representation of a free-play nonlinear system. Therefore, the FM method [26,27] is used in this work. The idea is that the local stiffness variations can be properly considered by the modes containing local significant deformations. This kind of modes can be obtained by adding a large mass to the local DOF.

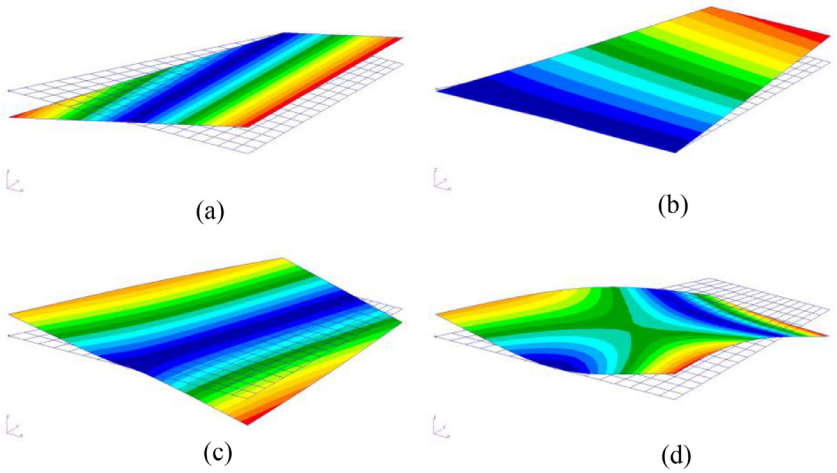

Fig. 6. FM modes, (a) the first mode (pitching mode), (b) the second mode (bending mode), (c) the third mode (torsion mode), (d) the fourth mode (second bending mode).

Table 1
Comparison of natural frequencies between the direct and FM methods for the normal stiffness and zero stiffness, unit: Hz.

	k = 100 N m/rad			k = 0 N m/rad		
Mode	Direct	FM	Error	Direct	FM	Error
1	43.2846	43.2846	0	0.0	0.0	0
2	86.2939	86.2939	0	53.0542	53.0542	0
3	293.4808	293.4808	0	293.0038	293.0039	0
4	370.3349	370.3362	0.0004%	352.2761	352.2839	0.0022%
5	584.6897	584.6903	0.0001%	583.5344	583.5384	0.0007%
6	846.8429	846.8656	0.0027%	836.8683	837.0396	0.0205%
7	1103.9460	1103.9715	0.0023%	1100.7520	1100.9577	0.0187%
8	1306.8380	1306.9380	0.0077%	1301.4330	1302.3263	0.0686%
9	1601.6170	1603.3325	0.1071%	1572.6300	1591.5522	1.2032%
10	1714.5850	6358.5389	–	1668.3580	3873.7392	–

To calculate the FM modes, a fictitious moment of inertia of 0.001 kg/m^2 is placed at the rotational DOF of the pitching axis where the free-play nonlinearity exists. This value is one order of magnitude larger than the moment of inertia of the wing about the pitching axis. The reference hinge stiffness value for the FM modal basis evaluation is k = 0 N m/rad.

The first 10 FM modes are chosen to represent the free-play system. Fig. 6 shows the four dominant FM modes and they denote the pitching mode, the bending mode, the torsion mode and the second bending mode, respectively. Table 1 lists the natural frequencies for the zero hinge stiffness and the normal hinge stiffness (k = 100 N m/rad). The results are calculated by both the direct method based on MSC.NASTRAN (Sol. 103) and the FM method. To obtain the natural frequency by the FM approach, the structural eigenvalue problem for Eq. (7) without the free-play and aerodynamic terms is solved [28].

The frequencies computed by the FM method show good agreement with the direct method except for the tenth mode. Note that the tenth mode contains local distortions and does not denote any natural mode [28,35]. The results demonstrate that this fictitious moment of inertia is appropriate and that it is reasonable to choose the FM modes as a constant modal space to represent the free-play nonlinear system.

3.2.2. Linear structural dynamics

The presented method used in the nonlinear analyses is also used in the linear analyses. But there are some differences between these two kinds of analyses. For linear analyses, the system contains only one subsystem and there is no switching point. The time step size used in linear analyses is a fixed value, while the nonlinear analyses use an adaptive time step.

A time-varying concentrated force which is perpendicular to the wing is exerted at the trailing edge of the tip chord and its expression is shown as (Unit: N):

$$F = 20\sin(100\pi t) \tag{11}$$

The hinge stiffness here is considered to be a constant value of 100 Nm/rad. The linear dynamic responses are calculated by both the direct method using MSC.NASTRAN (Sol. 109), and the FM method. To obtain the dynamic responses by the FM method, the concentrated harmonic load is projected to the modal basis. The time step is set to 5×10^{-5} s and Fig. 7 shows the time history of the rotational angle θ of the root mid-chord. Results show that the response computed by the FM

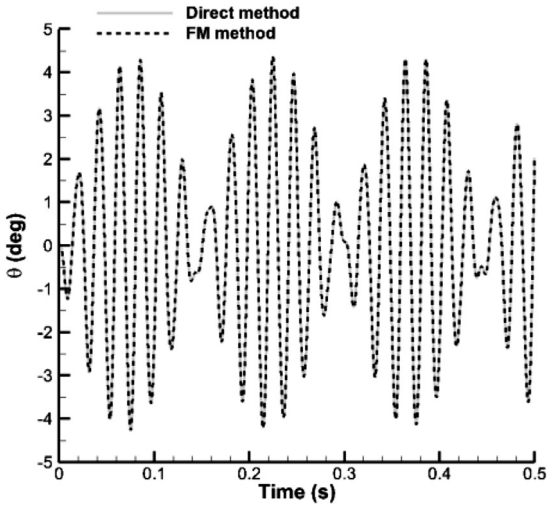

Fig. 7. Comparison of linear dynamic response between the direct method and FM method.

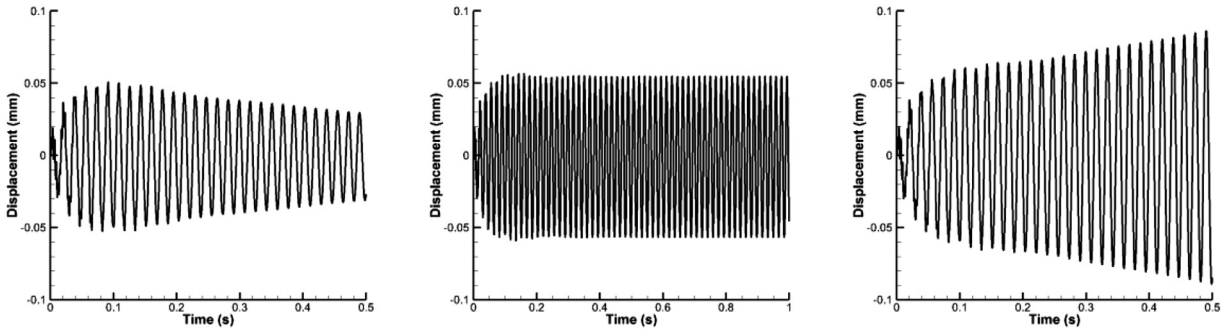

(a) $V = 139$ m/s (b) $V = 139.17$ m/s (c) $V = 139.3$ m/s

Fig. 8. Linear flutter computation, Ma = 0.6.

method is consistent with the direct method and reveal that the FM method can predict the dynamic response accurately for each linear subsystem of the free-play nonlinear system.

3.2.3. Linear flutter speed

In this section, the structural FM method is coupled with the CFD method to predict the linear flutter speed in time domain. The environment air density is 0.7364 kg/m^3. A typical subsonic Mach number of 0.6 is adopted. The flutter boundary at a specified Mach number is determined by changing the inflow velocity while keeping the density unvaried [47]. The environment temperature is allowed to be changed so that the speed of sound and the inflow velocity can be changed. The environment pressure is calculated according to the equation of the state of perfect gas. The flutter simulation is started after the steady CFD calculation is converged for the rigid wing. Because the wing is symmetric, the initial configuration coincides with the equilibrium position. To evaluate the flutter boundary, an initial disturbance is imposed on the wing.

The time step is set to 5×10^{-5} s. Fig. 8 plots the time histories of displacement of the monitor point located in the leading edge of the tip chord (Fig. 3), showing that the linear flutter speed at Mach 0.6 is 139.17 m/s. For comparison, the DLM in MSC.NASTRAN (Sol. 145) is also used to predict the linear flutter speed and it turns out to be 139.45 m/s. Therefore, the presented CFD/CSD coupling method shows good agreement with DLM in this subsonic Mach number.

Until now, the FM method has been validated for linear cases. Then, the nonlinear cases are discussed in the following sections.

3.3. Nonlinear aeroelastic analyses in subsonic flow

3.3.1. Validation of bisection method

The symmetric free-play is considered here and the free-play region is $-s < \theta < s$ ($s = 0.1°$), where s and $-s$ denote the switching points.

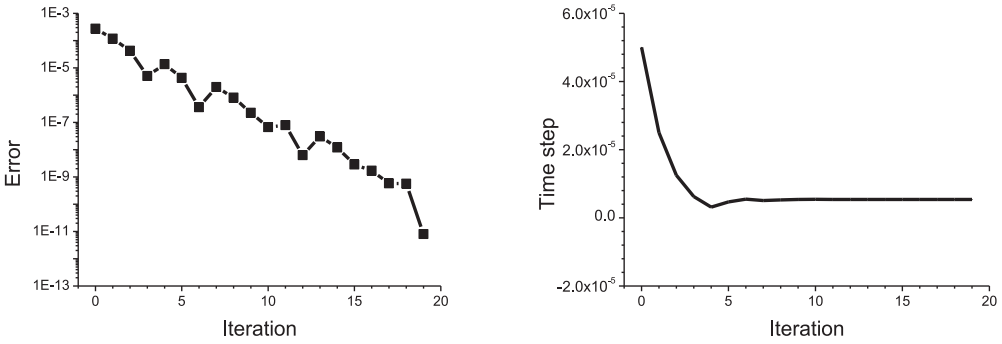

(a) Error in logarithmic scale (b) Convergence of adaptive time step

Fig. 9. Iterative process of catching switching point.

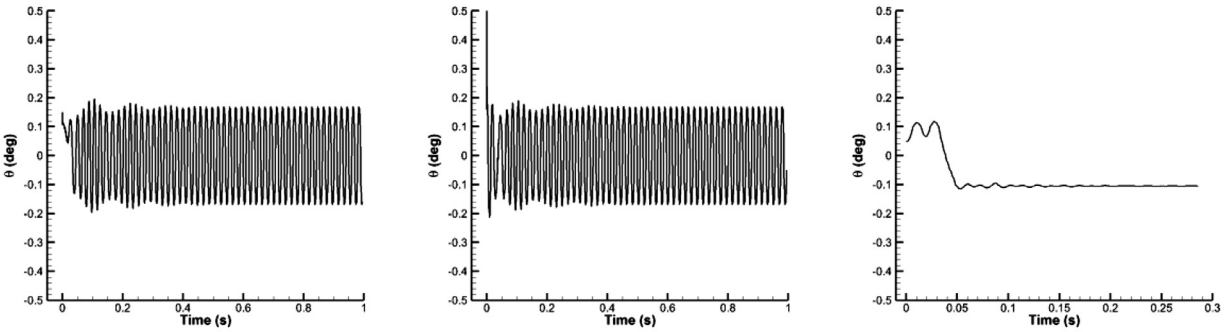

(a) $\theta_0 = 0.15°$ (b) $\theta_0 = 0.5°$ (c) $\theta_0 = 0.05°$

Fig. 10. Time histories of rotational angle under various initial conditions, $V = 105.4$ m/s.

If the subsystem does not change, the structural equations are integrated using the normal time step of 5×10^{-5} s. If the change in subsystem occurs, the bisection method is used to locate the switching point and determine the adaptive time step. To check the validity of this method, the concentrated force in Eq. (11) is exerted and the tolerance is set to 10^{-10}. Fig. 9 shows the iterative process of catching the switching point when it is crossed for the first time. As shown in Fig. 9a, the error is defined as the difference between θ and the switching point, and it reduces to the tolerance of 10^{-10} after 19 iterations. Fig. 9b plots the convergence history of the adaptive time step. These results demonstrate that the bisection method is effective for catching the switching point.

3.3.2. LCO prediction and hysteresis phenomenon

To evaluate aeroelastic LCOs, the whole wing is initially pitched by an angle θ_0. The Mach number is 0.6 and the free-stream velocity is set to 105.4 m/s which is below the linear flutter speed. Fig. 10 plots the dynamic responses of the rotational angle θ of the root mid-chord under various initial conditions. If the initial condition θ_0 is set to 0.15° or 0.5° (Fig. 10a-b) corresponding to setting θ_0 outside the free-play zone, the system tends to evolve into a stable oscillation after a short transient process, indicating the stable LCO occurs, whose amplitude is 0.169°.

The first four generalized displacements of the LCO are depicted in Fig. 11, which shows the LCO is dominated by the first three modes, while the fourth generalized displacement is very small. Other generalized displacements are also very small and not shown in the figure. It is seen that the generalized displacement has high order frequency components, which is different from a linear analysis at flutter boundary where only simple harmonic motions are observed.

The fast Fourier transform (FFT) analysis of the rotational angle θ is shown in Fig. 12. The fundamental frequency is 51.7 Hz. Higher order harmonics are also observed although their amplitudes are small compared with the fundamental harmonic. The FFT plot shows that the frequencies of the high order harmonics are about three times, five times and seven times the fundamental frequency. This observation is consistent with the work of Liu and Dowell [13], who studied an airfoil with free-play and showed the evidence of high order harmonics. According to Liu and Dowell [13], for periodic motions, high order harmonics need to be included in the harmonic balance analysis if their components are significant. But in the present case, the amplitudes of the high order harmonics are negligible, indicating the equivalent linearization method including only one harmonic can be used to predict the LCO for this flow velocity. The equivalent linearization method and the comparison with CFD/CSD coupling are discussed in Section 3.3.4.

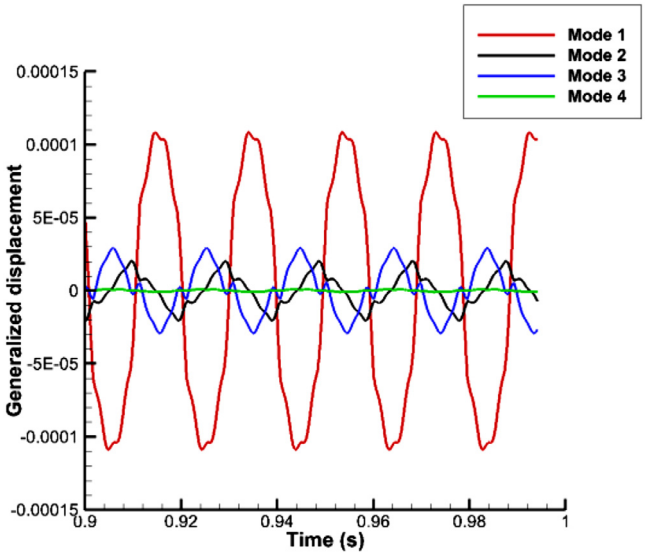

Fig. 11. Generalized displacements of the LCO.

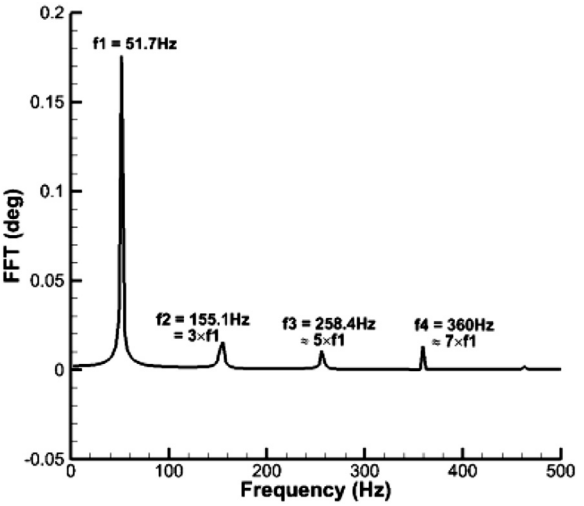

Fig. 12. FFT analysis of rotational angle, $V = 105.4$ m/s.

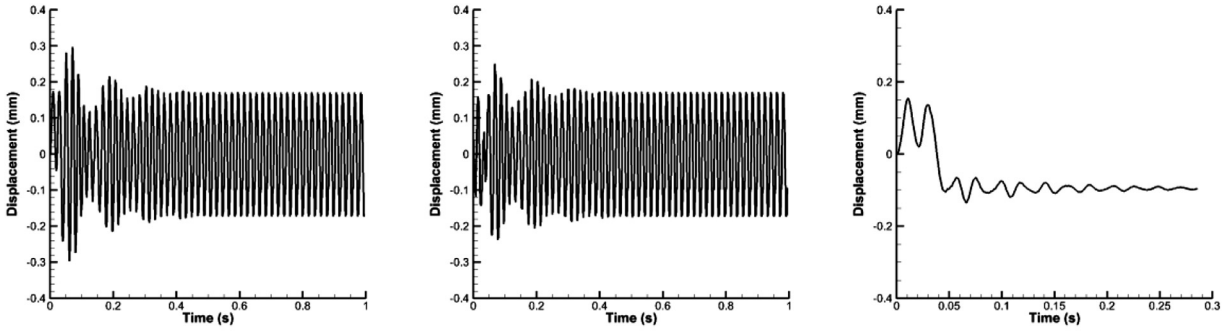

(a) $\theta_0 = 0.15°$ (b) $\theta_0 = 0.5°$ (c) $\theta_0 = 0.05°$

Fig. 13. Time histories of monitor point displacement under various initial conditions, $V = 105.4$ m/s.

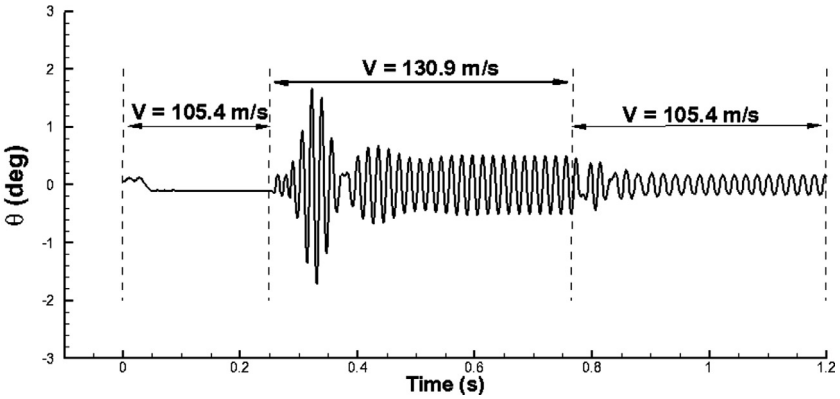

Fig. 14. Hysteresis phenomenon, $\theta_0 = 0.05°$.

Fig. 13 plots the monitor point displacement under the various initial conditions. If the initial condition θ_0 is set to 0.15° or 0.5° (Fig. 13a-b), the displacement response is attracted to the LCO whose amplitude is about 0.171 mm.

From the standpoint of energy, the system dissipates energy outside the free-play zone because the velocity is less than the linear flutter speed. On the other hand, when the system falls into the free-play zone, it will gain energy due to the instability of the subsystem with zero stiffness. Therefore, the nonlinear system will continually gain and lose energy during the switching of subsystems. If the equilibrium between the energy gaining and dissipation can be maintained, then the stable LCO arises [41]. But that does not mean the LCO occurs in any condition. Note that the stable LCO in Fig. 10a-b is excited by sufficiently large initial condition. If θ_0 decreases to 0.05° corresponding to setting θ_0 into the free-play zone, the monitor point displacement is damped (Fig. 13c) and the rotational angle converges to −0.105° near one of the free-play limits (Fig. 10c), indicating that the LCO behavior of the current nonlinear system is subcritical and that there exists an unstable LCO which cannot be predicted by the present time domain method.

The subcritical LCO behavior is characterized by hysteresis [49]. For example, a hysteresis phenomenon is shown in Fig. 14. The response starts with a relatively small velocity ($V = 105.4$ m/s) and with a small initial condition ($\theta_0 = 0.05°$). The preceding discussion has shown this initial condition cannot lead to a stable LCO. Then the flow velocity increases to 130.9 m/s and a stable LCO is discovered whose amplitude is 0.506°. After this LCO is developed, the velocity decreases back to 105.4 m/s and then the stable LCO with a relatively small amplitude is observed. It is seen that the LCO at $V = 105.4$ m/s may or may not develop depending on the previous motion history (hysteresis). The previous LCO with a large amplitude corresponds to having a large initial condition (disturbance) for the subsequent simulation, so that the subsequent LCO can be excited when the velocity decreases. The hysteresis phenomenon means that once a stable LCO occurs, the amplitude decreases as the flow speed decreases. It does not decay to zero until the flow speed is reduced below the LCO boundary, which is discussed in the next section.

Figs. 15 and 16 depict the phase plots of fully developed LCOs for the rotational angle and the monitor point displacement at various free-stream velocities. To better evaluate the effect of flow speed increasing, Fig. 17a and b combine the phase plots into a single plot for the rotational angle and the monitor point displacement, respectively.

3.3.3. LCO boundary

The free-play nonlinearity leads to LCOs even if the flow velocity is lower than the flutter boundary. To eliminate LCOs, the flow velocity should be less than the critical speed below which LCOs will not occur under any initial disturbance. This critical speed is called the LCO boundary in this paper. To determine the LCO boundary, the initial condition should be set to a sufficient large value, otherwise the subcritical property may suppress the occurrence of LCO. Then, the LCO boundary is determined by changing the flow velocity until the lowest velocity for the onset of LCO is found.

For example, as shown in Fig. 18, the initial condition is set to $\theta_0 = 0.5°$ corresponding to five times the free-play angle ($s = 0.1°$). It is seen that the response converges to an equilibrium position for the velocity less than 102 m/s. To ensure the LCO will not occur below 102 m/s, larger disturbances are applied as shown in Fig. 19. The velocity is set to 101.5 m/s. Results show that the response also converges under the initial conditions of $\theta_0 = 0.8°$ and $\theta_0 = 1.5°$. Therefore, the initial condition of $\theta_0 = 0.5°$ can be considered as a sufficient large disturbance. Further increase of the initial value will not affect the LCO calculation. Since the LCO begins to occur at $V = 102$ m/s, this critical speed is considered as the LCO boundary at Mach 0.6.

To evaluate the effect of free-play angle on the LCO boundary, the free-play angle is increased to $s = 0.5°$ as shown in Fig. 20. Results show that the LCO boundary for s = 0.5° still is 102 m/s, indicating the LCO boundary does not vary with the free-play angle.

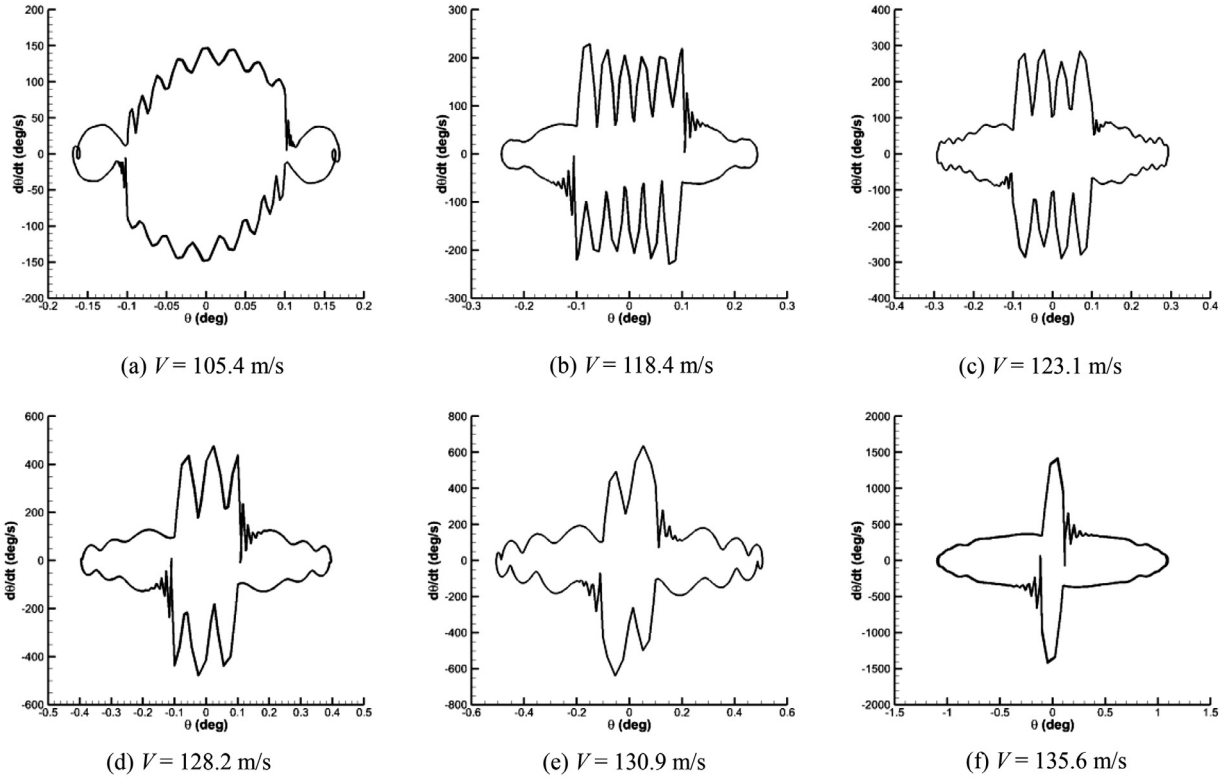

(a) $V = 105.4$ m/s (b) $V = 118.4$ m/s (c) $V = 123.1$ m/s

(d) $V = 128.2$ m/s (e) $V = 130.9$ m/s (f) $V = 135.6$ m/s

Fig. 15. Phase plots for θ at various speeds.

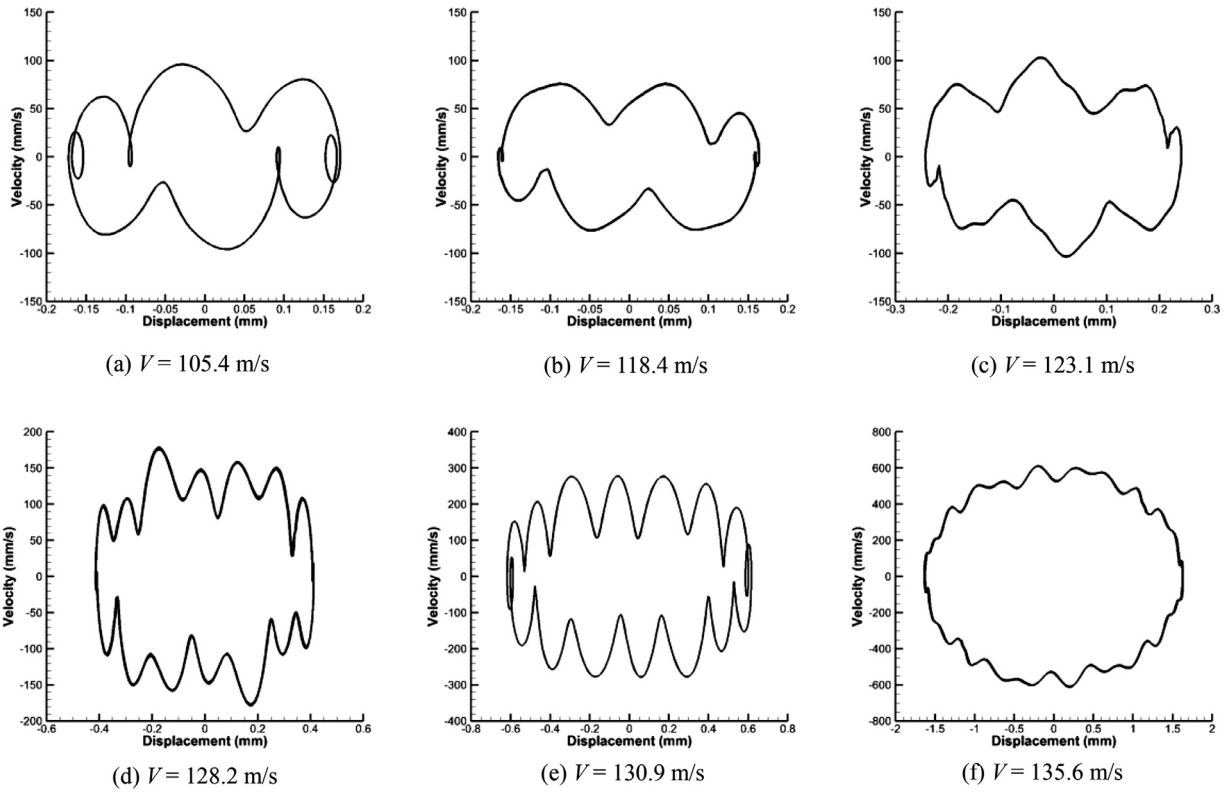

(a) $V = 105.4$ m/s (b) $V = 118.4$ m/s (c) $V = 123.1$ m/s

(d) $V = 128.2$ m/s (e) $V = 130.9$ m/s (f) $V = 135.6$ m/s

Fig. 16. Phase plots for monitor point displacement at various speeds.

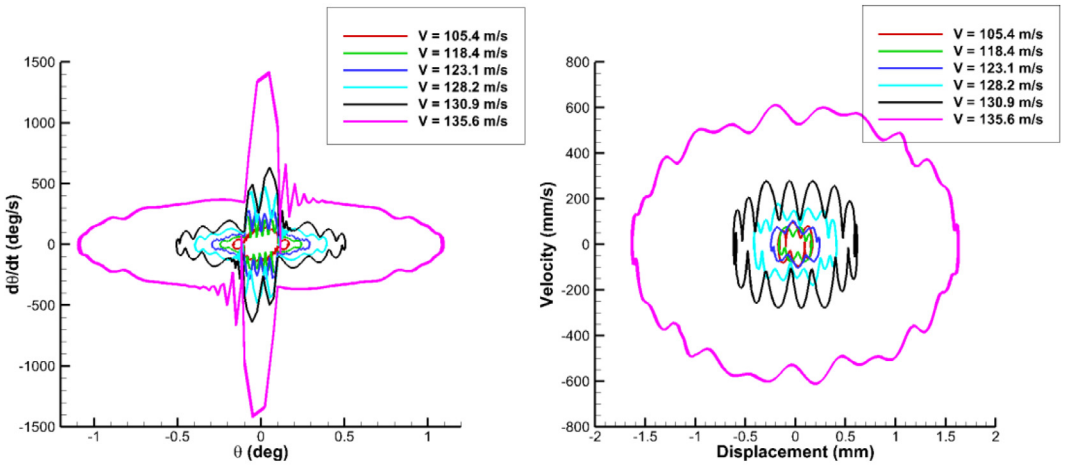

Fig. 17. Phase plots at various speeds in a single plot, (a) rotational angle θ, (b) monitor point displacement.

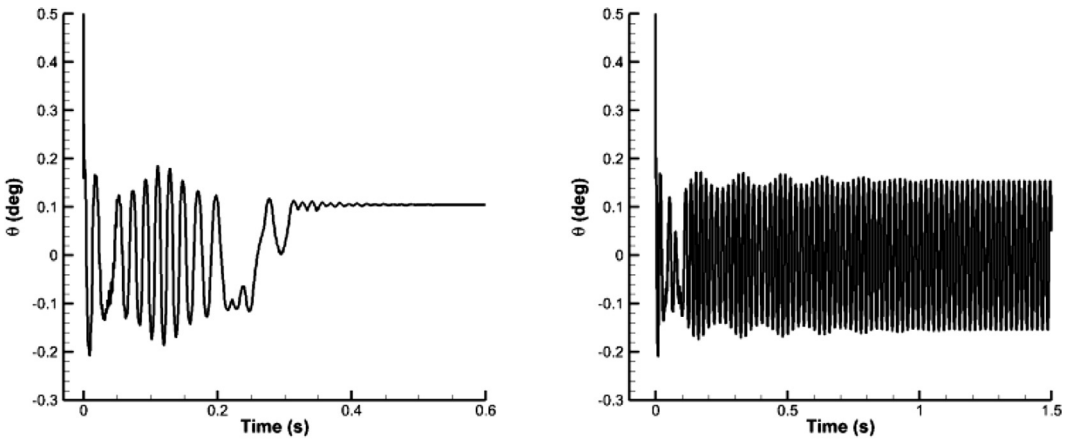

Fig. 18. LCO boundary calculation, Ma = 0.6, $\theta_0 = 0.5°$, $s = 0.1°$.

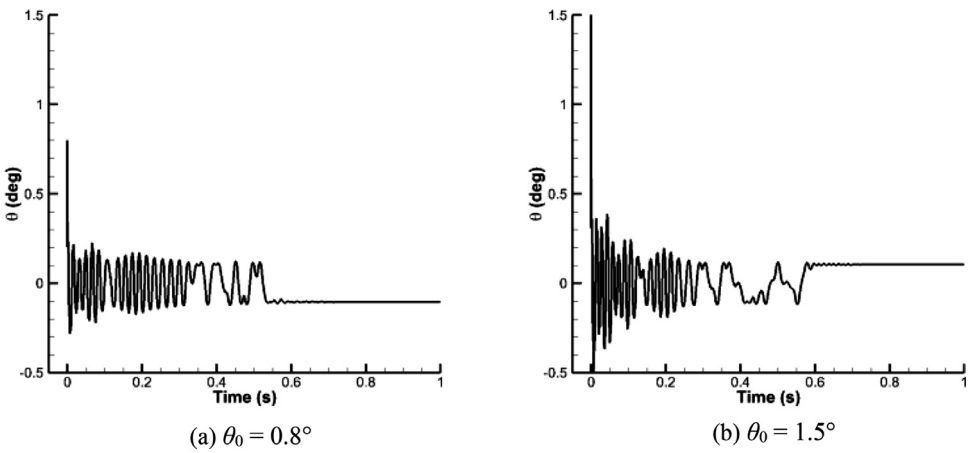

Fig. 19. Time responses under different initial conditions, Ma = 0.6, $V = 101.5$ m/s, $s = 0.1°$.

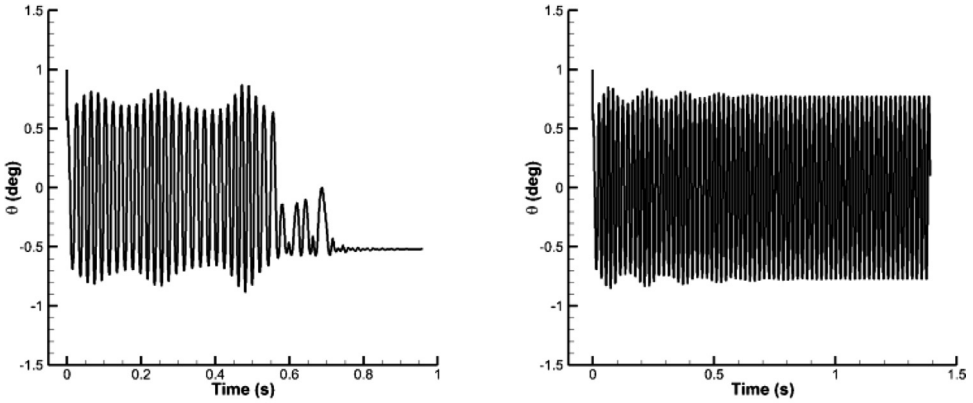

(a) $V = 101.5$ m/s (b) $V = 102$ m/s

Fig. 20. LCO boundary calculation, Ma = 0.6, $\theta_0 = 1.0°$, the free-play angle is increased to $s = 0.5°$.

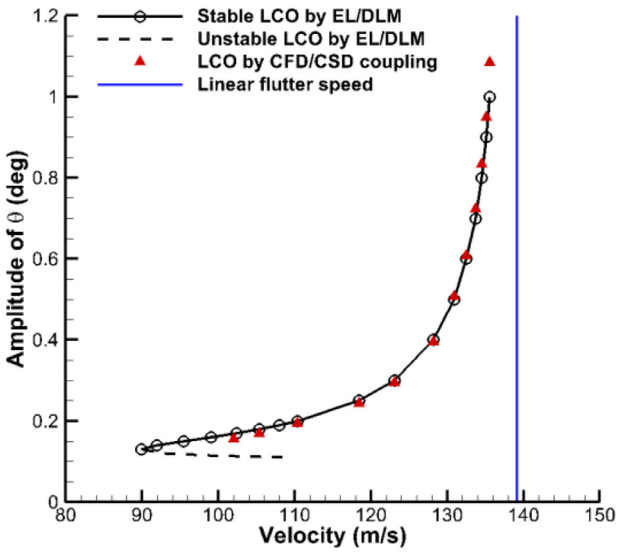

Fig. 21. LCO amplitude versus velocity, Ma = 0.6.

3.3.4. Comparison with equivalent linearization

In this section, the equivalent linearization method is used to predict the LCOs. Based on the describing function theory [6,37], the equivalent linearized structural stiffness is

$$K_{eq} = \begin{cases} 0, & A < s \\ \dfrac{2k}{\pi}\left[\dfrac{\pi}{2} - \arcsin\dfrac{s}{A} - \dfrac{s}{A}\sqrt{1-\left(\dfrac{s}{A}\right)^2}\right], & A \geq s \end{cases} \tag{12}$$

where A denotes the amplitude of θ and k represents the normal stiffness out of the free-play zone. After the equivalent stiffness is obtained for a given amplitude, the p-k method based on DLM in MSC.NASTRAN is used to calculate the flutter speed. This technique of equivalent linearization/doublet lattice method (EL/DLM) is used to obtain the curve of amplitude versus flow velocity as shown in Fig. 21. Note that the model given by Eq. (12) is only used in the linearized approach EL/DLM, while the proposed CFD/CSD coupling approach based on the FM method and the bisection method never uses this model.

EL/DLM is a frequency domain method and can predict both the stable LCOs (denoted by solid line) and the unstable LCOs (denoted by dash line). The LCO stability is determined by checking if the perturbed motion about the LCO is to return to the periodic orbit or leave away from it [5]. For the equivalent linearization method, this is equivalent to evaluate the change of sign of the real part of the eigenvalue for a perturbed amplitude [7]. This eigenvalue is obtained by the solution of the characteristic equations in the p-k method. An inference is that the LCO stability can be deter-

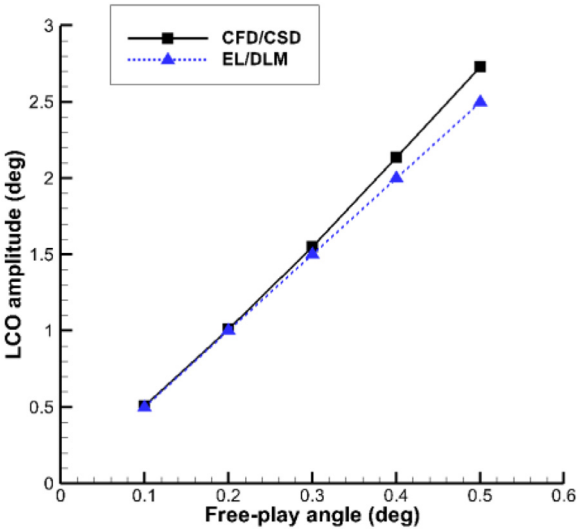

Fig. 22. LCO amplitude versus free-play angle, $V = 130.9$ m/s.

mined by the trend of the LCO amplitude with respect to the flow velocity [10,50–52]. If the amplitude increases with the increase of velocity, then the LCO is stable. If the amplitude decreases with the increase of velocity, then the LCO is unstable.

In Fig. 21, the turning point that connects the stable branch and the unstable branch denotes the smallest velocity for the onset of LCO. Thus, the LCO boundary (also called the turning point velocity) predicted by EL/DLM at Mach 0.6 is 89.9 m/s.

The results predicted by the CFD/CSD coupling are also presented for comparison. Note that the LCOs that can be simulated in time domain are stable. For the stable LCOs (Fig. 21), the amplitude calculated by the CFD/CSD coupling agrees well with that predicted by EL/DLM except for the speeds near the linear flutter boundary near which small changes in velocity can lead to large changes in LCO amplitude.

It is noted from Fig. 21 that there is a difference in LCO boundary between the two approaches. Similar observation was reported by Padmanabhan et al. [52], who studied the aeroelastic LCO behavior with cubic nonlinearity in incompressible flow. Their results showed that the stable LCO branch predicted by the equivalent linearization theory could not be confirmed by time marching in the vicinity of the turning point. In the work of Verstraelen et al. [18], experiments on a typical aeroelastic system with free-play were conducted in a low-speed wind tunnel and the experimental results were compared with mathematical predictions. Their results showed that the equivalent linearization theory predicted the LCOs at speeds lower than the experimental LCO onset velocity. This kind of deviation is likely due to the reason that the equivalent linearization theory is based on the assumption of simple harmonic motion so that it is not accurate enough for LCO predictions in some cases, such as the aperiodic responses, LCOs with multiple dominant frequencies and so on [25,29]. To improve the LCO solutions, Chen et al. [53] and Liu et al. [54] used the incremental harmonic balance method with high order harmonics to predict LCO behaviors and the critical speed for stable LCOs was shown to be consistent with time domain numerical results. But their studies were limited to 2-D airfoils in incompressible flow. To ensure the stable LCO prediction accuracy for 3-D structures in general compressible flow, especially near the turning point, this paper recommends the presented CFD/CSD coupling method.

The simulation using the CFD/CSD coupling is computationally expensive. For example, to obtain a fully developed LCO, the aeroelastic response in Fig. 10(a) is simulated for one second that includes enough periods. This simulation is based on parallel computing using 48 processes and the results show the CPU time is about 88 hours. What's more, several cases are needed to obtain the LCO boundary. Note that this high computational effort is a common feature in CFD applications. In contrast, the LCO response obtained by the linearized approach EL/DLM is based on serial computing and the CPU time is only a few seconds. Although the CFD/CSD coupling is less efficient than EL/DLM, it shows better performance in the prediction of LCO boundary, especially in transonic conditions.

As expressed in Eq. (12), K_{eq} is determined by the ratio of s to A. Based on the theory of EL/DLM, the flow speed at which LCO occurs is determined by K_{eq}, so the flow speed is determined by s/A, indicating the LCO amplitude is proportional to the free-play angle at a given flow speed. Fig. 22 shows the LCO amplitude of θ at various free-play angles at $V = 130.9$ m/s for the two methods. The amplitude calculated by the presented CFD/CSD coupling is also proportional to the free-play angle, which is consistent with EL/DLM, although there is a slight difference in the slope of curve between them. The FFT analyses are illustrated with Fig. 23, showing the free-play angle has little effect on the frequencies of the harmonic components.

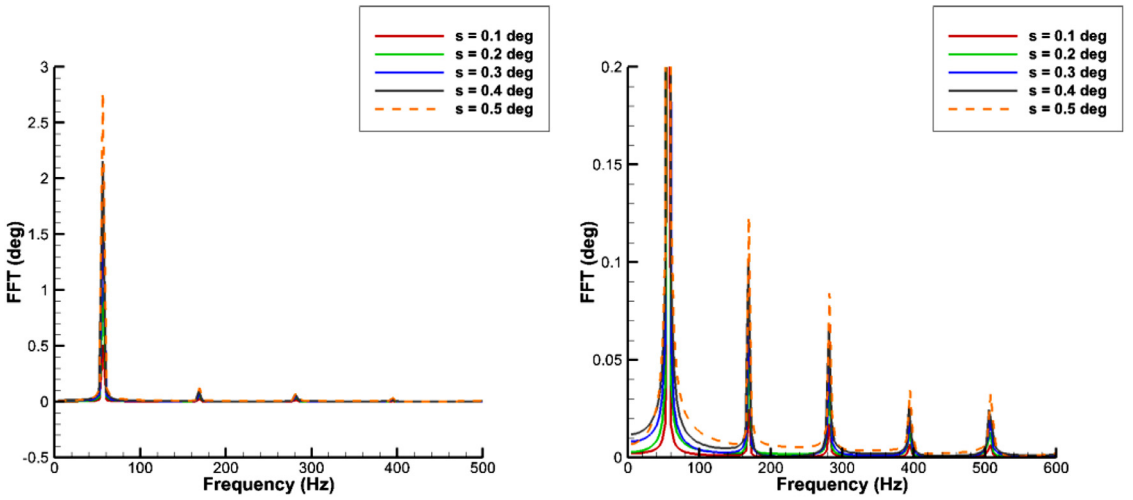

Fig. 23. FFT analyses for various free-play angles, $V = 130.9$ m/s.

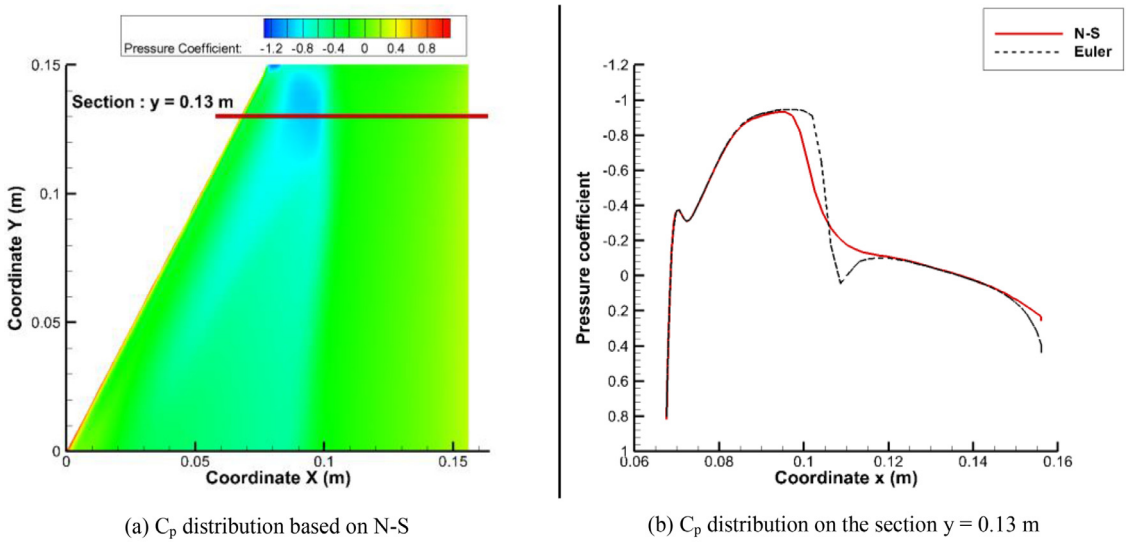

Fig. 24. Pressure coefficient distribution, Ma = 0.85, V =112.2 m/s, $\alpha = 0°$.

3.4. Nonlinear aeroelastic analyses in transonic flow

3.4.1. Comparison between N-S, Euler and DLM

In this section, the Mach number increases to 0.85. Both N-S equations and Euler equations belong to CFD methods and are used in the simulations. The viscous effect (e.g. boundary layer and shock-boundary layer interaction) can be considered by the N-S equations, while Euler equations are based on the inviscid hypothesis. Fig. 24a shows the steady pressure coefficient (C_p) distribution on the rigid wing surface and it is seen that the shock wave exists. Fig. 24b plots the comparison of C_p distribution on the section of y = 0.13 m, showing that there exists a difference near the shock wave and the shock wave predicted by the N-S equations moves forward compared to the Euler equations. Thus the viscous effect plays an important role in the transonic aerodynamic model.

Before the nonlinear aeroelastic discussions, the linear flutter results are presented. The predicted flutter speed at Ma 0.85 is 119 m/s, 124.7 m/s and 130.25 m/s for the Euler equations, N-S equations and DLM, respectively. The results show that it is non-conservative to determine the transonic flutter speed by DLM, while the Euler approach gives a too conservative result. Due to the existence of shock wave, the flow field is mixed subsonic-supersonic and this transonic flow is nonlinear even under the assumption of small disturbances [55]. The aerodynamic nonlinearity due to shock wave has a great impact on the flutter predictions [49]. Because DLM is based on the linear aerodynamic theory, it cannot accurately

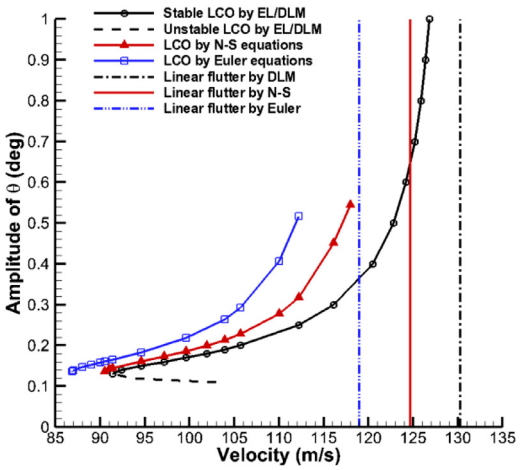

Fig. 25. LCO amplitude versus velocity, Ma = 0.85.

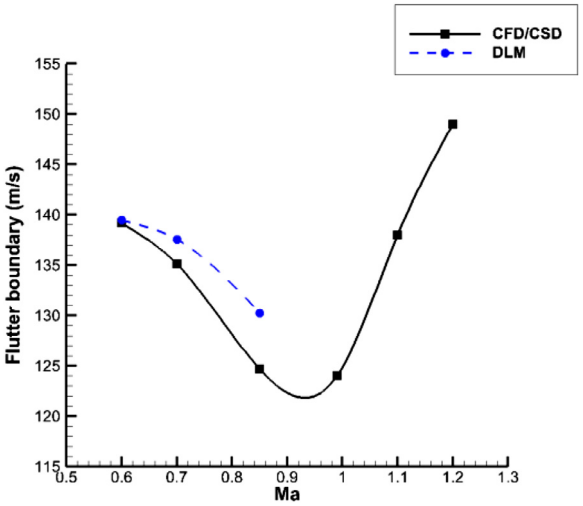

Fig. 26. Transonic dip in linear flutter boundary.

predict the transonic flutter speed. Although the Euler equations can capture the shock wave, this approach neglects the viscous term and gives a lower flutter speed compared to the N-S equations.

Then, the free-play nonlinear aeroelastic simulations are performed at this transonic Mach number. The symmetric free-play is still considered in this section and the free-play angle is set to $s = 0.1°$. All aeroelastic simulations are performed at zero angle of attack. Fig. 25 depicts the LCO amplitude of θ as a function of velocity for different methods. The linear flutter speeds are indicated by vertical lines. The comparison shows that DLM not only predicts the largest flutter speed but also predicts the largest velocity for a given LCO amplitude. In other words, DLM underestimates the LCO amplitude for a specified velocity. For the aerodynamic nonlinear methods, the Euler equations predict the largest LCO amplitude for a specified velocity. The LCO boundary is 86.9 m/s for the Euler equations, while it is 90.5 m/s for the N-S equations. Fig. 25 shows that the curve of LCO amplitude versus velocity is moved to a smaller velocity for the Euler method than the N-S method. This can be anticipated from the fact that the flutter speed obtained by the Euler equations is less than that obtained by the N-S equations. Therefore, it is conservative to use the nonlinear inviscid method to predict the flutter boundary, LCO boundary and LCO amplitudes. In other words, this comparison reveals that the presence of viscous effect shifts the LCO amplitude to a larger flow velocity.

3.4.2. Transonic dip phenomenon

First, the linear flutter boundary is calculated at various Mach numbers. The comparison between DLM and the CFD/CSD coupling is shown in Fig. 26. In this section, the N-S equations are used in the CFD/CSD coupling simulations. Because DLM is based on the linear aerodynamic theory, it deviates from the CFD/CSD coupling results as the Mach number approaches the sonic value. The aerodynamic nonlinearity due to shock wave can lead to the well-known transonic dip phenomenon

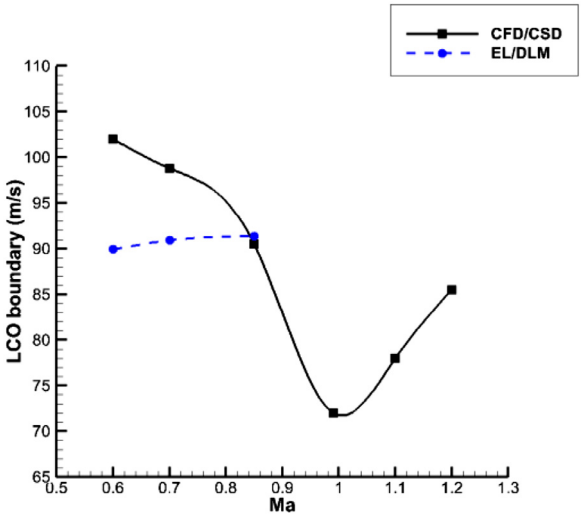

Fig. 27. Transonic dip in LCO boundary.

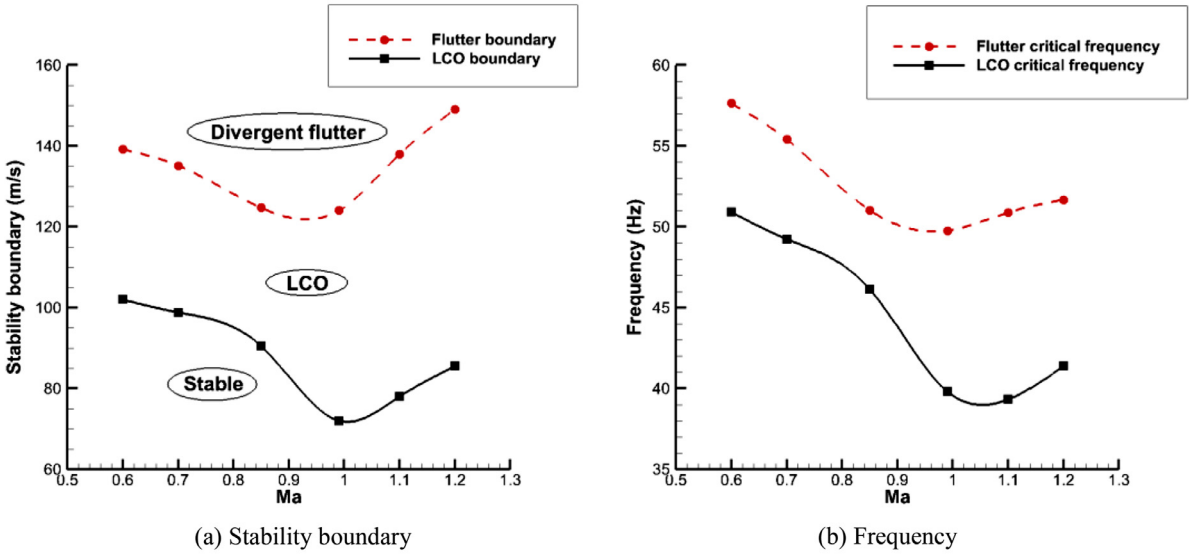

Fig. 28. Flutter boundary and LCO boundary.

[56–61] that the flutter speed experiences a drop within the transonic regime. Fig. 26 shows that the transonic dip in flutter boundary is well captured by the CFD/CSD coupling method.

Then, the LCO boundary of the free-play aeroelastic system is calculated at various Mach numbers and the comparison between EL/DLM and CFD/CSD coupling is shown in Fig. 27. It is seen that the LCO boundary predicted by EL/DLM is nearly unchanged over the range of Mach numbers. On one hand, the preceding discussion has shown that EL/DLM cannot predict the LCO boundary accurately even in subsonic regime because the assumption of simple harmonic motion is not accurate enough near the turning point. On the other hand, DLM is unsuitable for the calculation of transonic aerodynamic forces. Thus EL/DLM fails to predict the trend of LCO boundary with respect to Mach number and it is not recommended for stability boundary analyses of 3-D aeroelastic systems with free-play. In contrast, the CFD/CSD coupling results confirm that there is a transonic dip in the LCO boundary, which can be attributed to the free-play nonlinearity and the transonic aerodynamic nonlinearity. This phenomenon is similar to the transonic dip in linear flutter boundary but this new transonic dip is deeper due to the free-play nonlinear effect.

Fig. 28a plots the curves of flutter boundary and LCO boundary versus Mach number, which divide the figure into three zones. The LCO can be observed over a wide range of speed that ranges from the LCO boundary to the flutter boundary. If the flow velocity exceeds the flutter boundary, the response is divergent or has a large oscillation amplitude [37,53]. Although the LCOs with large amplitudes may occur in this region, this paper still adopts the terminology in Ref. [38] and calls it

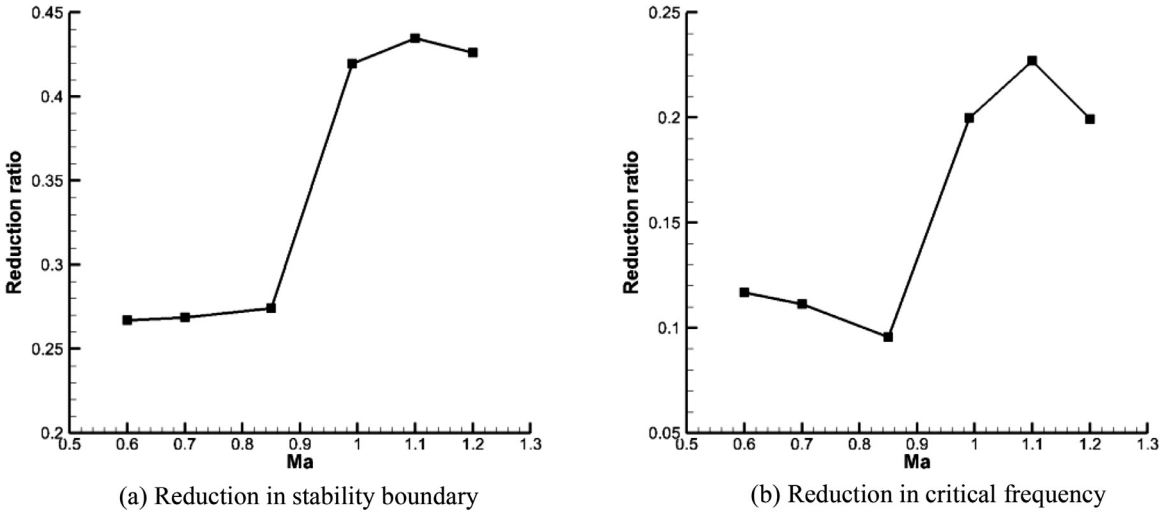

Fig. 29. Reduction ratio at various Mach numbers.

divergent flutter. If the flow velocity is below the LCO boundary, the response is damped under any initial disturbance. As shown in Fig. 28b, the flutter critical frequency and the LCO critical frequency also experience a drop in the transonic region.

Due to the free-play nonlinearity, both the stability boundary and the critical frequency are reduced significantly. To evaluate the free-play nonlinear effect on the transonic dip phenomenon, Fig. 29 plots the reduction ratio versus Mach number for the stability boundary and the critical frequency. The reduction ratio is defined as:

$$\text{reduction ratio} = \frac{\text{flutter value} - \text{LCO value}}{\text{flutter value}} \tag{13}$$

It is seen that the reduction ratio increases greatly near the transonic dip. This is because the flutter value is relatively low and the difference between the flutter and LCO values is large in the transonic region. The maximum reduction ratio turns out to be 43.5% for the stability boundary and 22.7% for the critical frequency, respectively. Both maximums occur at Mach 1.1.

As discussed in Section 3.3.4, the LCO amplitude is in proportion to the free-play angle. In other words, if LCO occurs at a certain velocity, the change in free-play angle only affects the LCO amplitude and cannot eliminate the occurrence of LCO. It can be deduced that the size of free-play angle has no effect on the LCO boundary. The results in Section 3.3.3 (Figs. 18 and 20) confirm this conclusion. Since the LCO boundary does not vary with the free-play angle, the transonic dip and the reduction ratio are not affected by the free-play angle.

4. Conclusion

This paper proposes a framework of CFD/CSD coupling that can consider both the free-play nonlinearity and aerodynamic nonlinearity for three dimensional aeroelastic analyses. The reduced structural equations of motion are constructed using the FM method and are solved with the aid of bisection method that can detect the switching point effectively and accurately. The RBF method is used for the fluid-structure interpolation and CFD mesh motion. The reduced structural equations and the CFD solver are coupled in a loosely coupling manner. The three dimensional all-movable wing with free-play in pitch is studied in subsonic and transonic conditions. The results are as follows.

This CFD/CSD coupling method is shown to predict the LCOs and the hysteresis phenomenon in time domain effectively. In subsonic flow, the LCO amplitude predicted by the CFD/CSD coupling is in good agreement with that predicted by the linearized approach EL/DLM, except for the speeds near the flutter boundary and the LCO boundary. The CFD/CSD coupling shows better performance in the prediction of LCO boundary than EL/DLM, which is based on the assumption of simple harmonic motion but not accurate enough near the turning point.

In transonic flow, the aerodynamic nonlinearity due to shock wave leads to the significant difference in LCO amplitudes between the CFD/CSD coupling and EL/DLM. The comparison between N-S and Euler results shows that the viscous effect increases both the LCO boundary and the flutter boundary and shifts the LCO amplitude to a larger flow velocity.

Because the LCO behavior is subcritical, a large initial disturbance is needed to find the LCO boundary. At a specified Mach number, the LCO boundary is determined by changing the flow velocity until the critical speed is found. The transonic dip in LCO boundary is observed by the CFD/CSD coupling, while EL/DLM fails to predict this phenomenon. This transonic dip phenomenon is caused by the free-play nonlinearity and the transonic aerodynamic nonlinearity. From the results of this study, the LCO boundary and the critical frequency can be at most 43.5% and 22.7% below the flutter boundary and the flutter frequency, respectively. The LCO boundary is not affected by the free-play angle.

This paper studies the free-play induced LCOs in subsonic and transonic flows. However, some aerodynamic nonlinear mechanisms, such as the strong shock wave interference and the shock-boundary layer interaction, are still difficult and remain unresolved. Future work should focus on the strong aerodynamic nonlinear effects on the free-play aeroelastic behaviors.

Declaration of Competing Interest

The authors declare that they have no known competing financial interests or personal relationships that could have appeared to influence the work reported in this paper.

CRediT authorship contribution statement

Chengde Huang: Conceptualization, Methodology, Software, Validation, Formal analysis, Writing - original draft, Visualization. **Jie Huang:** Writing - original draft, Visualization. **Xin Song:** Writing - original draft, Visualization. **Guannan Zheng:** Writing - review & editing, Supervision, Project administration. **Guowei Yang:** Writing - review & editing, Supervision, Project administration, Funding acquisition.

Acknowledgment

This work was supported by National Natural Science Foundation of China (No. 11702298 and No. 11672303).

References

[1] D. Tang, E.H. Dowell, Aeroelastic response induced by free play, Part 1: theory, AIAA J. 49 (11) (2011) 2532–2542, doi:10.2514/1.J051055.
[2] P.C. Chen, E. Ritz, Nonlinear flutter analysis for the scaled F-35 with horizontal-tail free play, J. Aircr. 51 (3) (2014) 883–889, doi:10.2514/1.C032501.
[3] Z.C. Yang, L.C. Zhao, Analysis of limit cycle flutter of an airfoil in incompressible flow, J. Sound Vib. 123 (1) (1988) 1–13, doi:10.1016/S0022-460X(88)80073-7.
[4] S. He, Z.C. Yang, Y.S. Gu, Limit cycle oscillation behavior of transonic control surface buzz considering free-play nonlinearity, J. Fluids Struct. 61 (2016) 431–449, doi:10.1016/j.jfluidstructs.2015.11.014.
[5] M. Manetti, G. Quaranta, P. Mantegazza, Numerical evaluation of limit cycles of aeroelastic systems, J. Aircr. 46 (5) (2009) 1759–1769, doi:10.2514/1.42928.
[6] J.S. Bae, D.J. Inman, I. Lee, Effects of structural nonlinearity on subsonic aeroelastic characteristics of an aircraft wing with control surface, J. Fluids Struct. 19 (2004) 747–763, doi:10.1016/j.jfluidstructs.2004.04.005.
[7] J.T. Gordon, E.E. Meyer, R.L. Minogue, Nonlinear stability analysis of control surface flutter with free-play effects, J. Aircr. 45 (6) (2008) 1904–1916, doi:10.2514/1.31901.
[8] B.H.K. Lee, A. Tron, Effects of structural nonlinearities on flutter characteristics of the CF-18 aircraft, J. Aircr. 26 (8) (1989) 781–786, doi:10.2514/3.45839.
[9] D.B. Kholodar, Nature of freeplay-induced aeroelastic oscillations, J. Aircr. 51 (2) (2014) 571–583, doi:10.2514/1.C032295.
[10] Z.C. Yang, S. He, Y.S. Gu, Transonic limit cycle oscillation behavior of an aeroelastic airfoil with free-play, J. Fluids Struct. 66 (2016) 1–18, doi:10.1016/j.jfluidstructs.2016.07.013.
[11] B.H.K. Lee, L. Liu, K.W. Chung, Airfoil motion in subsonic flow with strong cubic nonlinear restoring forces, J. Sound Vib. 281 (2005) 699–717, doi:10.1016/j.jsv.2004.01.034.
[12] B. Ghadiri, M. Razi, Limit cycle oscillations of rectangular cantilever wings containing cubic nonlinearity in an incompressible flow, J. Fluids Struct. 23 (2007) 665–680, doi:10.1016/j.jfluidstructs.2006.10.010.
[13] L. Liu, E.H. Dowell, Harmonic balance approach for an airfoil with a freeplay control surface, AIAA J. 43 (4) (2005) 802–815, doi:10.2514/1.10973.
[14] S. Fichera, S. Ricci, Freeplay-induced limit-cycle oscillations in a t-tail: numerical vs experimental validation, J. Aircr. 52 (2) (2015) 486–495, doi:10.2514/1.C032748.
[15] H.H. Dai, X.K. Yue, J.P. Yuan, D. Xie, S.N. Atluri, A comparison of classical Runge-Kutta and Henon's methods for capturing chaos and chaotic transients in an aeroelastic system with freeplay nonlinearity, Nonlin. Dyn. 81 (2015) 169–188, doi:10.1007/s11071-015-1980-x.
[16] D. Asjes, A. Diwadkar, U. Vaidya, A. Kelkar, Development and system analysis of a two-dimensional rotational freeplay nonlinearity model, J. Aircr. 53 (3) (2016) 860–864, doi:10.2514/1.C033275.
[17] W.J. Al-Mashhadani, E.H. Dowell, H.R. Wasmi, A.A. Al-Asadi, Aeroelastic response and limit cycle oscillations for wing-flap-tab section with freeplay in tab, J. Fluids Struct. 68 (2017) 403–422, doi:10.1016/j.jfluidstructs.2016.11.017.
[18] E. Verstraelen, G. Dimitriadis, G.D.B. Rossetto, E.H. Dowell, Two-domain and three-domain limit cycles in a typical aeroelastic system with freeplay in pitch, J. Fluids Struct. 69 (2017) 89–107, doi:10.1016/j.jfluidstructs.2016.11.019.
[19] D.A. Pereira, R.M.G. Vasconcellos, M.R. Hajj, F.D. Marques, Effects of combined hardening and free-play nonlinearities on the response of a typical aeroelastic section, Aerosp. Sci. Technol. 50 (2016) 44–54, doi:10.1016/j.ast.2015.12.022.
[20] R.D. Firouz-Abadi, S.M. Alavi, H. Salarieh, Analysis of non-linear aeroelastic response of a supersonic thick fin with plunging, pinching and flapping free-plays, J. Fluids Struct. 40 (2013) 163–184, doi:10.1016/j.jfluidstructs.2013.03.019.
[21] D.B. Kholodar, Aircraft control surface and store freeplay-induced vibrations in aeroelastic stability envelope, J. Aircr. 53 (5) (2016) 1538–1548, doi:10.2514/1.C033772.
[22] D.K. Kim, J.S. Bae, I. Lee, J.H. Han, Dynamic model establishment of a deployable missile control fin with nonlinear hinge, J. Spacecr. Rockets 42 (1) (2005) 66–77, doi:10.2514/1.3608.
[23] N. Yang, N. Wang, X. Zhang, W. Liu, Nonlinear flutter wind tunnel test and numerical analysis of folding fins with freeplay nonlinearities, Chin. J. Aeronaut. 29 (1) (2016) 144–159, doi:10.1016/j.cja.2015.12.011.
[24] N.K. Banavara, J.R. Newsom, Framework for aeroservoelastic analyses involving nonlinear actuators, J. Aircr. 49 (3) (2012) 774–780, doi:10.2514/1.C031246.
[25] G.H.C. Silva, G.D.B. Rossetto, G. Dimitriadis, Reduced-order analysis of aeroelastic systems with freeplay using an augmented modal basis, J. Aircr. 52 (4) (2015) 1312–1325, doi:10.2514/1.C032912.
[26] M. Karpel, C.D. Wieseman, Modal coordinates for aeroelastic analysis with large local structural variations, J. Aircr. 31 (2) (1994) 396–403, doi:10.2514/3.46499.
[27] M. Karpel, C.D. Wieseman, Time simulation of flutter with large stiffness changes, J. Aircr. 31 (2) (1994) 404–410, doi:10.2514/3.46500.

[28] R. Huang, H.Y. Hu, Y.H. Zhao, Nonlinear aeroservoelastic analysis of a controlled multiple-actuated-wing model with free-play, J. Fluids Struct. 42 (2013) 245–269, doi:10.1016/j.jfluidstructs.2013.06.007.
[29] J.S. Bae, S.M. Yang, I. Lee, Linear and nonlinear aeroelastic analysis of fighter-type wing with control surface, J. Aircr. 39 (4) (2002) 697–708, doi:10.2514/2.2984.
[30] P. Gold, M. Karpel, Reduced-size aeroservoelastic modeling and limit-cycle-oscillation simulations with structurally nonlinear actuators, J. Aircr. 45 (2) (2008) 471–477, doi:10.2514/1.28933.
[31] J.S. Bae, D.K. Kim, W.H. Shin, I. Lee, S.H. Kim, Nonlinear aeroelastic analysis of a deployable missile control fin, J. Spacecr. Rockets 41 (2) (2004) 264–271, doi:10.2514/1.1052.
[32] S.K. Paek, I. Lee, Flutter analysis for control surface of launch vehicle with dynamic stiffness, Comput. Struct. 60 (4) (1996) 593–599, doi:10.1016/0045-7949(95)00425-4.
[33] W.H. Shin, I. Lee, Y.S. Shin, J.S. Bae, Nonlinear aeroelastic analysis for a control fin with an actuator, J. Aircr. 44 (2) (2007) 597–605, doi:10.2514/1.24721.
[34] J.Y. Kim, K.S. Kim, I. Lee, Y.K. Park, Transonic aeroelastic analysis of all-movable wing with free play and viscous effects, J. Aircr. 45 (5) (2008) 1820–1824, doi:10.2514/1.37435.
[35] I. Lee, S.H. Kim, Aeroelastic analysis of a flexible control surface with structural nonlinearity, J. Aircr. 32 (4) (1995) 868–874, doi:10.2514/3.46803.
[36] K.A. Kousen, O.O. Bendiksen, Limit cycle phenomena in computational transonic aeroelasticity, J. Aircr. 31 (6) (1994) 1257–1263, doi:10.2514/3.46644.
[37] S. He, Z.C. Yang, Y.S. Gu, Nonlinear dynamics of an aeroelastic airfoil with free-play in transonic flow, Nonlin. Dyn. 87 (4) (2017) 2099–2125, doi:10.1007/s11071-016-3176-4.
[38] D.H. Kim, I. Lee, Transonic and low-supersonic aeroelastic analysis of a two-degree-of-freedom airfoil with a freeplay non-linearity, J. Sound Vib. 234 (5) (2000) 859–880, doi:10.1006/jsvi.2000.2907.
[39] D.P. Jones, I. Roberts, A.L. Gaitonde, Identification of limit cycles for piecewise nonlinear aeroelastic systems, J. Fluids Struct. 23 (2007) 1012–1028, doi:10.1016/j.jfluidstructs.2007.03.007.
[40] M.D. Conner, L.N. Virgin, E.H. Dowell, Accurate numerical integration of state-space models for aeroelastic systems with free play, AIAA J. 34 (10) (1996) 2202–2205, doi:10.2514/3.13377.
[41] Y.M. Chen, J.K. Liu, Nonlinear aeroelastic analysis of an airfoil-store system with a freeplay by precise integration method, J. Fluids Struct. 46 (2014) 149–164, doi:10.1016/j.jfluidstructs.2014.01.003.
[42] W. Tian, Z.C. Yang, Y.S. Gu, Dynamic analysis of an aeroelastic airfoil with freeplay nonlinearity by precise integration method based on Padé approximation, Nonlin. Dyn. 89 (2017) 2173–2194, doi:10.1007/s11071-017-3577-z.
[43] L. Liu, Y.S. Wong, B.H.K. Lee, Non-linear aeroelastic analysis using the point transformation method, Part 1: freeplay model, J. Sound Vib. 253 (2) (2002) 447–469, doi:10.1006/jsvi.2001.4064.
[44] T.C.S. Rendall, C.B. Allen, Unified fluid–structure interpolation and mesh motion using radial basis functions, Int. J. Numer. Methods Eng. 74 (10) (2008) 1519–1559, doi:10.1002/nme.2219.
[45] W. Liu, C.D. Huang, G.W. Yang, Time efficient aeroelastic simulations based on radial basis functions, J. Comput. Phys. 330 (2017) 810–827, doi:10.1016/j.jcp.2016.10.063.
[46] C.D. Huang, W. Liu, G.W. Yang, Numerical studies of static aeroelastic effects on grid fin aerodynamic performances, Chin. J. Aeronaut. 30 (4) (2017) 1300–1314, doi:10.1016/j.cja.2017.04.013.
[47] C.D. Huang, J. Huang, X. Song, G.N. Zheng, X.Y. Nie, Aeroelastic simulation using CFD/CSD coupling based on precise integration method, Int. J. Aeronaut. Space Sci. 21 (2020) 750–767, doi:10.1007/s42405-020-00248-9.
[48] T.C.S. Rendall, C.B. Allen, Efficient mesh motion using radial basis functions with data reduction algorithms, J. Comput. Phys. 228 (17) (2009) 6231–6249, doi:10.1016/j.jcp.2009.05.013.
[49] E. Jonsson, C. Riso, C.A. Lupp, C.E.S. Cesnik, J.R.R.A. Martins, B.I. Epureanu, Flutter and post-flutter constraints in aircraft design optimization, Prog. Aerosp. Sci. (2019) 109, doi:10.1016/j.paerosci.2019.04.001.
[50] J.P. Thomas, E.H. Dowell, K.C. Hall, Modeling viscous transonic limit-cycle oscillation behavior using a harmonic balance approach, J. Aircr. 41 (6) (2004) 1266–1274, doi:10.2514/1.9839.
[51] D.B. Kholodar, E.H. Dowell, J.P. Thomas, K.C. Hall, Limit-cycle oscillations of a typical airfoil in transonic flow, J. Aircr. 41 (5) (2004) 1067–1072, doi:10.2514/1.618.
[52] M.A. Padmanabhan, E.H. Dowell, C.L. Pasiliao, Computational study of aeroelastic limit cycles due to localized structural nonlinearities, J. Aircr. 55 (4) (2018) 1531–1541, doi:10.2514/1.C034645.
[53] Y.M. Chen, D.H. Chen, J.K. Liu, Subcritical limit cycle in airfoil aeroelastic system with freeplay: prediction and mechanism, AIAA J. 57 (10) (2019) 4482–4489, doi:10.2514/1.J058522.
[54] J.K. Liu, F.X. Chen, Y.M. Chen, Bifurcation analysis of aeroelastic systems with hysteresis by incremental harmonic balance method, Appl. Math. Comput. 219 (2012) 2398–2411, doi:10.1016/j.amc.2012.08.034.
[55] O.O. Bendiksen, Review of unsteady transonic aerodynamics: theory and applications, Prog. Aerosp. Sci. 47 (2) (2011) 135–167, doi:10.1016/j.paerosci.2010.07.001.
[56] F. Liu, J. Cai, Y. Zhu, H.M. Tsai, A.S.F. Wong, Calculation of wing flutter by a coupled fluid-structure method, J. Aircr. 38 (2) (2001) 334–342, doi:10.2514/2.2766.
[57] X.Y. Chen, G.C. Zha, M.T. Yang, Numerical simulation of 3-D wing flutter with fully coupled fluid–structural interaction, Comput. Fluids 36 (2007) 856–867, doi:10.1016/j.compfluid.2006.08.005.
[58] G.W. Yang, S. Obayashi, J. Nakamichi, Aileron buzz simulation using an implicit multiblock aeroelastic solver, J. Aircr. 40 (3) (2003) 580–589, doi:10.2514/2.3134.
[59] H. Ashley, Role of shocks in the "sub-transonic" flutter phenomenon, J. Aircr. 17 (3) (1980) 187–197, doi:10.2514/3.57891.
[60] K. Isogai, On the transonic-dip mechanism of flutter of a sweptback wing, AIAA J. 17 (7) (1979) 793–795, doi:10.2514/3.61226.
[61] K. Isogai, Transonic-dip mechanism of flutter of a sweptback wing: Part II, AIAA J. 19 (9) (1981) 1240–1242, doi:10.2514/3.7853.